Homogeneous Phase Distribution in Q-2D Perovskites via Co-Assembly of Spacer Cations for Efficient Light-Emitting Diodes

*Zhenyu Guo, Yin Liang, Dongyuan Ni, Liang Li, Shaocheng Liu, Yu Zhang, Qi Chen, Qing Zhang, Qian Wang, and Huanping Zhou**

Quasi-2D (Q-2D) perovskites are promising candidates to apply in light-emitting diodes (LEDs). However, delicate control on crystallization kinetics is needed to suppress severe phase segregation. Here, the crystallization kinetics of Q-2D perovskites are investigated via in situ absorbance spectroscopy and for the first time find the multiphase distribution is governed by the arrangement, rather than diffusion, of spacer cations at the nucleation stage, which associate with its assembling ability determined by molecular configuration. A "co-assembly" strategy is conceived by combining co-cations with different configuration characteristics, where bulky cations disturb the assembling between slender cations and lead–bromide sheet, contributing to homogeneous emitting phase with effective passivation. Correspondingly, in the phenylethylammonium (PEA$^+$)-based Q-2D perovskites ($<n> = 3$), homogeneous phase distribution is achieved by incorporating co-cation triphenylmethaneammonium (TPMA$^+$), the branching terminals of which suppress cations assembling into low-n phases and afford adequate cations as passivating ligands. Therefore, the champion external quantum efficiency of the LED device reaches 23.9%, which is among the highest performance of green Q-2D perovskite LEDs. This work reveals that the arrangement of spacer cations determines the crystallization kinetics in Q-2D perovskites, providing further guidance on the molecular design and phase modulation of Q-2D perovskites.

1. Introduction

Lead halide perovskites are emerging semiconductor materials with superior luminous performance due to high defect tolerance and high color purity, which has demonstrated tremendous potential in applications of LEDs,[1–9] laser,[10,11] and so on. Q-2D perovskites, featuring higher exciton binding energy and spatial confinement effect, are more conducive to radiative recombination, which is expected as promising emitting layers in LEDs.[5,12–20] Hitherto, the highest external quantum efficiency (EQE) of green and pure red perovskite LEDs has surpassed 25%, which unexceptionally utilizes Q-2D perovskites as emitting layer.[5,17,21–23] Thus, it is of great necessity to modulate the properties of Q-2D perovskites for superior device performance.

Essentially, Q-2D perovskites are self-assembled multiphase structure, where wide phase distribution with severe segregation takes place if lacking delicate control over the crystallization process, resulting in non-radiative recombination losses.[15,22,24–27] Narrow phase distribution with suppressed segregation has always been pursued superior luminescent performance.[5,21,23,26,28–30] Briefly, it is the different diffusion and crystallization rate between inorganic (lead halogen frameworks) and organic (spacer cations) components that account for the polydisperse distribution.[15,28,31–32] Thus, efforts have been focused on the modulation of spacer cations to acquire desired phase distributions. For example, 18-crown-6 (crown) is utilized to limit the aggregation of phenylethylammonium (PEA$^+$) through the interaction between $-NH_3^+$ and lone pair electrons of oxygen atoms in the crown.[21,33] Hydrogen bonding interaction between additives and spacer cations, like fluorine atoms and PEA$^+$,[5] methanesulfonate and butylammonium (BA$^+$),[34] is reported to promote the stacking growth of spacer-free nanosheet, realizing a more homogeneous phases distribution. Recently, spacer cations featuring different configuration characteristics (butylammonium, hexylammonium, PEA$^+$, and related derivatives) are utilized to fabricate 2D/3D heterojunctions, among which 3-fluoro-phenethylammonium (3F-PEA$^+$) exhibits lower

Z. Guo, Y. Liang, L. Li, S. Liu, Y. Zhang, Q. Zhang, H. Zhou
Beijing Key Laboratory for Theory and Technology of Advanced Battery Materials
Key Laboratory of Polymer Chemistry and Physics of Ministry of Education
School of Materials Science and Engineering
Peking University
Beijing 100871, China
E-mail: happy_zhou@pku.edu.cn
D. Ni, Q. Wang
School of Materials Science and Engineering
Peking University
Beijing 100871, China
Q. Chen
School of Materials Science and Engineering
Beijing Institute of Technology
Beijing 100081, P. R. China

**ADVANCED
SCIENCE NEWS**

www.advancedsciencenews.com

**ADVANCED
MATERIALS**

www.advmat.de

formation energy and preferential formation of higher order Q-2D perovskites on the surface of 3D perovskites, enabling effective surface passivation and carrier transport in perovskite solar cells simultaneously.[35] Although these works imply spacer cations play a vital role in the self-assembly of Q-2D perovskites, the underlying diffusion and arrangement behaviors of spacer cations along film processing are still unclear.[31] Furthermore, the understanding of the formation kinetics of different phases during film processing still lacks and the principle of modulation and selection of spacer cations is highly required to further promote the performance of Q-2D perovskite LEDs.

Herein, for the first time, we find that the multiphase distribution in Q-2D perovskites is governed by the arrangement, rather than diffusion, of spacer cations at the nucleation stage, which associate with its assembling ability determined by molecular configuration. On this basis, we conceive a "co-assembly" strategy by combining co-cations with different configuration characteristics, where bulky cations disturb the assembling between slender cations and lead–bromide sheet, contributing to a homogeneous emitting phase with effective passivation. Correspondingly, in the PEA$^+$-based Q-2D perovskites ($<n>$ = 3), the homogeneous phase distribution is achieved by incorporating co-cation triphenylmethaneammonium (TPMA$^+$), the branching alkyl terminals of which suppress cations assembling into low-n phases and afford adequate cations as passivating ligands. The photoluminescence quantum yield (PLQY) of the perovskite films significantly increase from 65.4% (PEA) to 81.2% (TPMA/PEA) and the EQE of the green LED device reach 23.9%, which is among the highest performance of green Q-2D perovskite LEDs. This work reveals that the arrangement of spacer cations is the key factor that determines the crystallization kinetics in Q-2D perovskites and unravels the principle of designing spacer cations to regulate phase distribution, providing further guidance on the modulation of Q-2D perovskites.

2. Results and Discussion

2.1. Assembling Ability of Spacer Cations and Impacts on Phase Distribution

We first assess the self-assembling behaviors between lead halogen frameworks and various bulky ammonium cations. The molecular structures of selected ammoniums are shown in **Figure 1**a, which exhibit gradually bulkier and more branching molecular configuration (IBA ‹ IPA ‹ tBA, DPPA ‹ DPEA ‹ TPMA, where IBA = isobutylamine, IPA = isopropylamine, tBA = tert-butylamine, DPPA = 3,3-diphenylpropylamine, DPEA = 2,2-diphenylethylamine and TPMA = triphenylmethylamine). We fabricated film samples from precursor solutions for 2D perovskites (n = 1, PbBr$_2$: ammonium bromides = 1: 2, mole ratio) and conducted X-ray diffraction (XRD) measurements. As shown in Figure 1b, well-indexed diffraction peaks emerge in the PEA, IBA, and IPA samples, which are assigned to (0k0) crystallographic planes of 2D perovskites (n = 1 phase).[14,24] The strongest diffraction peaks at 2θ = 5.32°, 6.32° and 7.54° belong to (020) plane of PEA, IBA, and IPA-derived 2D perovskites, respectively, according to which the interplanar spacing is calculated as 16.59, 13.97 and 11.71 Å, consistent with the size difference among these spacer cations (PEA$^+$ > IBA$^+$ > IPA$^+$). It is noteworthy that

neither signals of ammonium bromides nor PbBr$_2$ are observed for these three samples (Figure S1a, Supporting Information), indicating that PEA$^+$, IBA$^+$, and IPA$^+$ are well assembled as spacer layers between lead halogen frameworks in the 2D perovskites. Nevertheless, no periodic peaks of (0k0) are observed for tBA, DPPA, DPEA, and TPMA samples (Figure 1b). Meanwhile, the occurrence of diffraction peaks of these ammonium bromides and PbBr$_2$ indicate these ammoniums cannot intercalate into the lead halogen frameworks.[36] Ultraviolet-visible (UV–vis) absorption spectra (Figure S1b, Supporting Information) furthermore confirm the formation of n = 1 phase only in the PEA, IBA, and IPA samples. Therefore, we propose that the branching tails of ammonium cations pose difficulty in assembling into spacer layers.

Considering the various self-assembling behavior of these bulky ammonium cations, we sought to analyze the n-phase distribution accordingly in Q-2D perovskites. Perovskite films were fabricated from precursor solutions with a composition of $<n>$ = 3 Ruddlesden–popper (RP) perovskites (details in Experimental Section). As shown in absorption spectra (Figure 1c), absorption signals at 430, 460, and 480 nm, belonging to n = 2, 3, and 4 phases, respectively, are observed in PEA, IBA, and IPA-films ($<n>$ = 3).[14,24] However, as for the ammonium cations (tBA$^+$, DPPA$^+$, DPEA$^+$, and TPMA$^+$), which cannot form n = 1 phase (Figure 1b), no signals of low-dimensional ($n \leq 4$) perovskites emerge. Instead, absorption steps with less excitonic characteristics are observed at 530 ± 10 nm, which are assigned to n = ∞ phase or 3D perovskites. The absorption edge of tBA, DPEA, and TPMA-film exhibit obvious red-shift compared with PEA-film. We interpret this phenomenon as the steric hindrance caused by the bulky tails is so high that these cations can hardly bind with lead halogen frameworks firmly to confine the growth of perovskite crystals.[37] Besides, we post-treat the 3D FAPbBr$_3$ film with an isopropanol solution of alkyl ammonium bromides (the structure is described in Figure 1a) without annealing (Figure S2a, Supporting Information). As shown in photoluminescence (PL) spectra (Figure S2b,c, Supporting Information), a dominant PL peak belonging to n = 1 phase is observed in PEA$^+$-treated film, and its intensity is much stronger than that of the 3D phase at 540 nm, suggesting a strong tendency for PEA$^+$ to assemble into 2D perovskite. Meanwhile, the emissions of low-n (n = 2, 3, 4) phases with weaker intensity are also observed in the IBA$^+$ and IPA$^+$-treated films. However, no well-defined emission of low-n phases is observed in tBA$^+$, DPPA$^+$, DPEA$^+$, and TPMA$^+$-treated samples. Spacer cations have to arrange one by one regularly along with the lead halogen frameworks to form the 2D or low-n phases, where the −NH$_3^+$ terminal occupies the space of lead halogen frameworks through hydrogen and ionic bonding. However, the space of lead halogen frameworks is not large enough to accommodate the cations when the alkyl chain (−(CH$_2$)$_n$−NH$_3^+$) is very short, where tBA$^+$ is the typical example.[36] Besides, even though the alkyl chain of DPPA$^+$ (−CH$_2$−CH$_2$−CH$_2$−NH$_3^+$) and DPEA$^+$ (−CH$_2$−CH$_2$−NH$_3^+$) is long enough for them to bind with lead halogen frameworks, the alkyl terminals with two non-coplanar benzene rings pose a high steric hindrance for them to arrange one by one regularly along with the lead halogen plane. Therefore, the formation of low-n phases involves the chain length and steric hindrance of the alkyl terminal of the spacer cations.
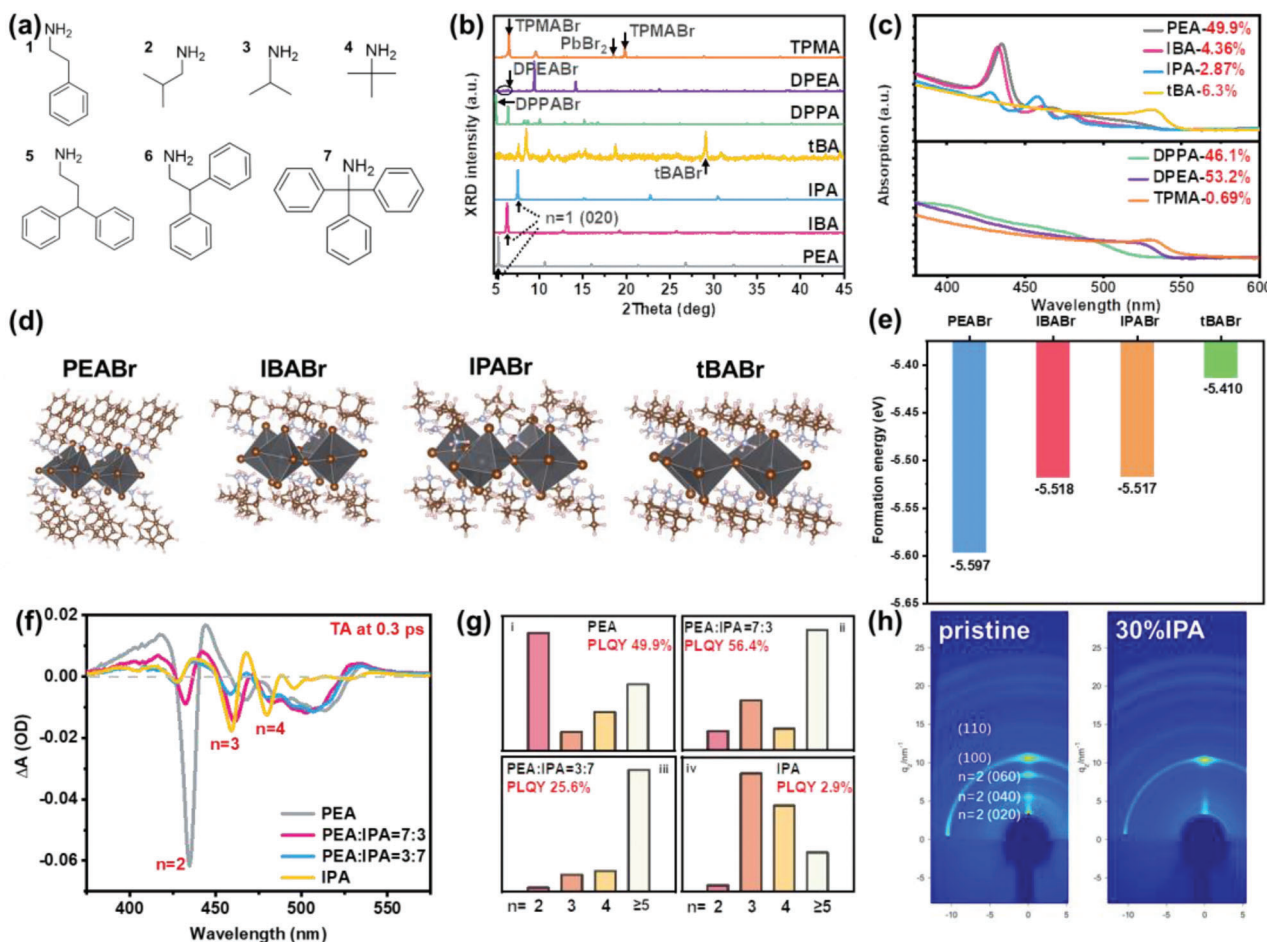
Figure 1. a) Spacer amines used in this work: 1, phenylethylamine (PEA); 2, isobutylamine (IBA); 3, isopropylamine (IPA); 4, tert-butylamine (tBA); 5, 3,3-diphenylpropylamine (DPPA); 6, 2,2-diphenylethylamine (DPEA); 7, triphenylmethylamine (TPMA). b) XRD patterns of film samples fabricated from precursor solutions containing ammonium bromide and $PbBr_2$ (mole ratio as 2:1). c) Absorption spectra of perovskite films from a precursor with bulky ammonium cations, FABr, and $PbBr_2$ (mole ration as 2:2:3, recipe for $<n>$ = 3 composition). d) Optimized structure of the 2D perovskites with different spacer cations. e) Calculated formation energies of the 2D perovskites with different spacer cations. f) Transient absorption spectrum of the Q-2D perovskite films at Δt = 0.3 ps. g) The relative contributions of different n phases in each film according to the integral intensity of GSB in the corresponding TA spectra. h) GIWAXS patterns of Q-2D perovskite with different components.

In addition, the formation energies of the 2D (n = 1) perovskites with different cations are calculated by using density functional theory (DFT, Experimental Section). As shown in Figure 1d,e, the formation energies of the 2D perovskites are in the order of $PEA^+ < IBA^+ < IPA^+ < tBA^+$, which means that PEA_2PbBr_4 is energetically favorable to form. On the other hand, the calculations for the $DPPA^+$, $DPEA^+$, and $TPMA^+$-based 2D perovskites are difficult to realize the convergence during the geometric optimization processes, which agree with our experimental results (Figure 1b) that $DPPA^+$, $DPEA^+$, and $TPMA^+$ cannot assemble into 2D perovskites (n = 1 phase). Based on the above discussion, these ammoniums are classified into three categories by their assembling ability into low-n phases, namely, strong (PEA^+), medium (IBA^+, IPA^+), and weak (tBA^+, $DPPA^+$, $DPEA^+$, and $TPMA^+$). In addition, we measure the PLQY of the samples derived from different ammonium cations (Figure 1c). Intriguingly, although a homogenous phase is achieved in weak assembling cation-derived films (tBA^+ and $TPMA^+$), those with shorter chains achieve unexpectedly low PLQY (6.3% for tBA^+ and 0.69%

for $TPMA^+$, respectively), which is due to their incapability to serve as passivating ligands because of bulky tails. In addition, although low-n phases barely exist in DPPA and DPEA samples, no appreciable improvement in PLQY (46.1% for $DPPA^+$ and 53.2% for $DPEA^+$, respectively) is observed compared with PEA-film. This is attributed to the branching tails of $DPPA^+$ and $DPEA^+$ that are unable to passivate the emitting phases as effectively as PEA^+. Meanwhile, samples with medium assembling ability (IBA^+ and IPA^+) exhibit only 4.36% and 2.87%, respectively, which is attributed to the weak confinement effect for small size without benzene ring and its polydisperse phase distribution.[26] Therefore, it seems that homogeneous phase distribution and decent ligands passivation cannot be ensured simultaneously with one type cation, necessitating the adjustment of assembling ability by combining cations from two categories for better luminescent properties.

Hence, we substitute PEA^+ partly by medium assembling IPA^+ (0, 30%, 70%, and 100%) in the $<n>$ = 3 recipes and fabricate Q-2D perovskite films to investigate the evolution of

phase distribution. Transient absorption (TA) spectroscopy was acquired to precisely analyze the n-phase distribution.[28,35,38,39] We plotted the absorption curves when the delay time between the pump and probe light is 0.3 ps, during which the energy transfer has not happened and the intensity of PB peaks represents the populations of corresponding phases. As shown in the spectra (Figure 1f), there are three prominent photobleaching (PB) peaks in the 440–490 nm range, ascribed to $n = 2$, 3, and 4 phases, respectively. The relative content of different phases is further calculated by integrating these PB peaks and the results are shown in the histogram (Figure 1g). The method to calculate the relative contributions of different phases is described in Experimental Section. In the pristine film with PEA$^+$ as spacer cations (i), severe segregation in the n-phase distribution is observed, where $n = 2$ and $n \geq 5$ phases account for the major part. It was documented that excess low-n phases consume too many spacer cations to leave the emitting phase ($n \geq 5$) unpassivated, leading to a PLQY of only 49.9%.[28] As IPA$^+$ substitute 30% of PEA$^+$ (ii), the amount of $n = 2$ phases sharply decrease and a higher PLQY of 56.4% is achieved, which is ascribed to that more spacer cations are available to passivate the emitting phases ($n \geq 5$ phases). When more IPA$^+$ are included, low-n phases decrease further (iii, 70%IPA) and even a gradient distribution form (iv, 100%IPA), but the PLQY conversely decreases to only 25.6% and 2.9%, respectively. We propose that the size of IPA$^+$ is not bulky enough to confine the growth of perovskite, weakening the otherwise strong confinement effect in the PEA$^+$ system. Furthermore, the multiphase composition with $n = 3$, 4, and ≥ 5 phases in (iv) results in poor energy transfer and non-radiative recombination losses.[26] Grazing incidence wide-angle X-ray scattering (GI-WAXS) (Figure 1h) further confirms that the scattering rings at $q = 2.83$, 5.58, 8.4 nm^{-1} in the pristine film (100%PEA) is significantly attenuated when IPA$^+$ substitute, which belongs to (0k0) crystallographic planes of $n = 2$ phases.[14,24] Therefore, phase distribution greatly changes along with the assembling ability of spacer cations, which is adjusted by combining cations with different configuration characteristics.

2.2. Phases Formation Kinetics in Q-2D Perovskites

It is intriguing to know how IPA$^+$, which possesses quite different configuration characteristics from PEA$^+$, affects the assembly between spacer cations and lead halogen frameworks, resulting in different n-phase distribution. Thus, we analyzed the formation kinetics of different phases during film deposition via an in situ absorbance spectroscopy (Experimental Section). **Figure 2**a,b depict the evolution of absorbance during the spin coating process (60 s), during which anti-solvent chlorobenzene (CB) is dropped at the 26th second (Experimental Section). Absorption of $n = 2$, 3, and ≥ 5 phases (at 430 ± 5, 450 ± 5, and $\geq$490 nm, respectively) are immediately observed after anti-solvent dripping, indicating the formation of different-n phases. The corresponding absorption over time is displayed in Figure S3a,b (Supporting Information). Meanwhile, the substitution of IPA$^+$ obviously decreases the absorption of $n = 2$ phase, indicating the formation of fewer $n = 2$ phase. Besides, it is noteworthy that the absorption of all phases almost remains constant throughout the spin coating process, indicat-

ing the number of different phases is unchanged during this period.

The evolution of film during annealing (90 °C for 3 min) is also explored via in situ absorbance spectroscopy (Figure 2c,d). The corresponding absorption over time is displayed in Figure S3c,d (Supporting Information). It is shown that the intensity and position of absorption of $n = 2$ and 3 phases remain unchanged, signifying that annealing does not influence the quantity of low-n phases. The above in situ measurements tell the facts that the amount of low-n ($n = 2$ and 3) phases is determined at the moment when anti-solvent dropping and remains unchanged during the subsequent spin coating and annealing. Since solvent dimethyl sulfoxide (DMSO) is extracted swiftly by the anti-solvent when applying the one-step method to fabricate Q-2D perovskite films, nucleation is considered to prevail right after anti-solvent dropping and growth dominates the annealing process.[24] Therefore, we suggest it is the swift nucleation that determines the amount of low-n ($n = 2$ and 3) phases, while the subsequent growth during annealing has a negligible impact on it. In addition, a red shift is observed for the absorption edge of $n = \infty$ (Figure 2c,d; Figure S3c,d, Supporting Information), which is ascribed to the increased grain size and weakened quantum confinement effect. As for the growth of $n = \infty$ phase during annealing, we interpret the formation and coalescence of high-dimensional perovskite blocks as much easier in the absence of spacer cations. Furthermore, when only reducing 30% PEA$^+$ in the recipe (PEA$^+$: IPA$^+$: FA$^+$ = 0.7: 0: 1, mole ratio), the absorption of $n = 2$ phase is still higher compared to the IPA$^+$ substituting sample (PEA$^+$: IPA$^+$: FA$^+$ = 0.7: 0.3: 1, mole ratio) (detailed composition in Figure S4, Supporting Information), which indicate nucleation of fewer low-n phases is due to different assembling behaviors of PEA$^+$ rather than the change in the quantity of PEA$^+$.

The nucleation of Q-2D perovskites involves the precipitation of organic (spacer cations) and inorganic (lead halogen framework) components, among which PEA$^+$ is reported as prone to aggregation, leading to the formation of low-n phases and severe phase segregation. Hence, we propose the underlying mechanism of the mixing spacer cations strategy is to influence the nucleation state by disturbing and retarding the assembly between lead halogen frameworks and spacer cations, reducing the nucleation of low-n phases and alleviating the segregation in phase distribution. As vividly shown in the Figure 2g, although IPA$^+$ can act as spacer cations to form low-n phases, the assembly of PEA$^+$ is partly interrupted by the incorporation of IPA$^+$, restricting the formation of low-n phases and affording more available organic ligands (PEA$^+$ and IPA$^+$) as passivator to bind with the surface of emitting phases (high-n phases). To be noted, the peak position of low-n phases absorption shifts to shorter wavelengths after incorporating IPA$^+$, because IPA$^+$ weakens the coupling effect between the π-electron (PEA$^+$) and p orbital of halogen, further confirming the assembling of IPA$^+$ into spacer layers[40] (Figure S5, Supporting Information). According to the above analysis, we attempt to realize a homogeneous phase distribution through the co-assembly of spacer cations from the two different categories classified above, where bulky cations suppress the aggregation of spacer cations and slender cations serve as passivating ligands of emitting phases.
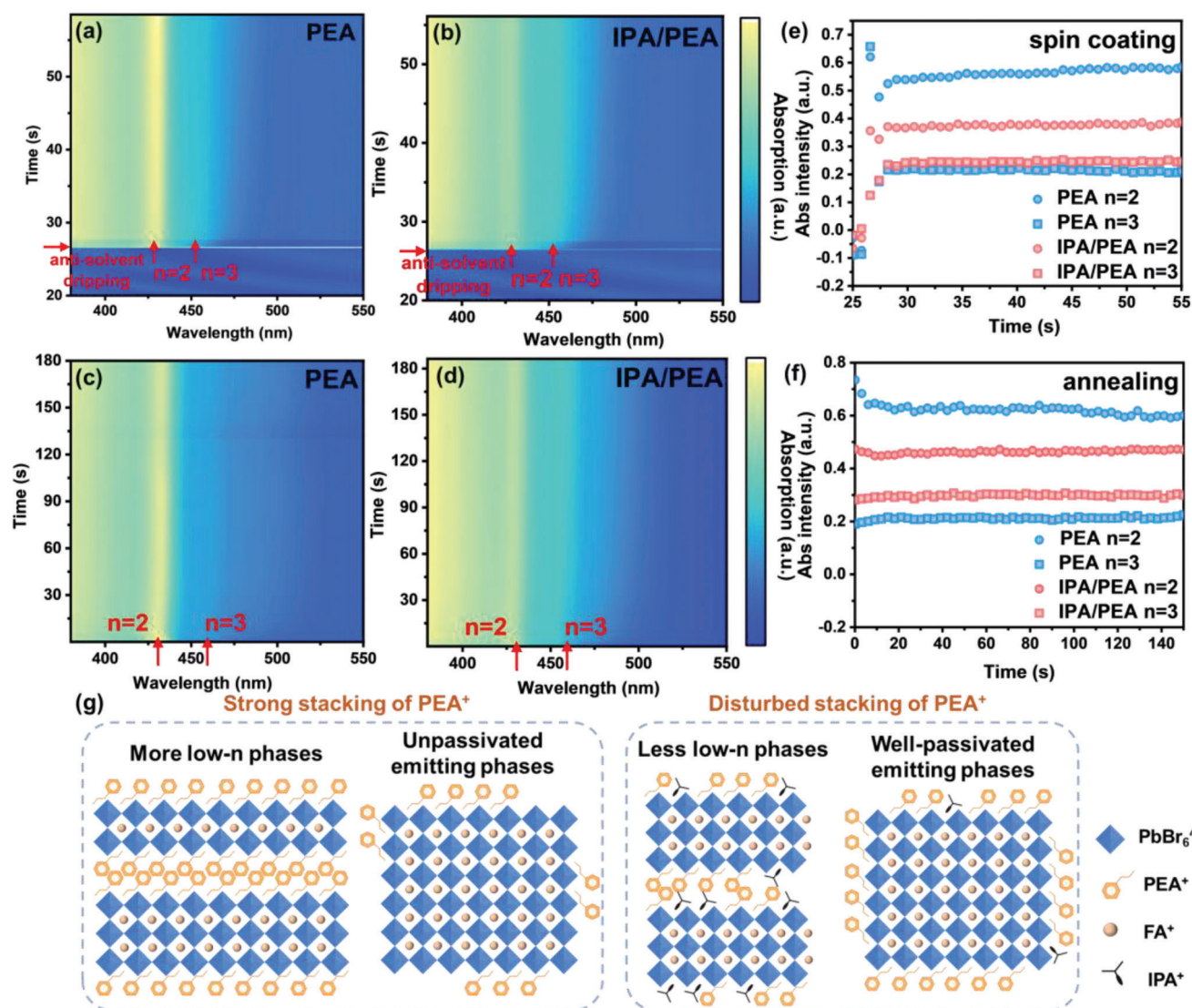
**ADVANCED
SCIENCE NEWS**

www.advancedsciencenews.com

**ADVANCED
MATERIALS**

www.advmat.de

Figure 2. a–d) In situ absorbance measurement of Q-2D perovskites during spin coating (a,b) and annealing (c,d) process. e,f) Evolution of absorption of $n = 2$ and 3 phases over time during spin coating (e) and annealing (f) process. g) Schematic diagram of the impacts of spacer cations with different sizes and configurations on n-phase distribution in Q-2D perovskites.

2.3. Rational Modulation of Phase Distribution via Bulkier Cations

Based on the proposed mechanism, we seek to modulate nucleation state and phase distribution through the substitution of 30% PEA^+ by cations with even weaker assembling ability ($DPPA^+$, $DPEA^+$, and $TPMA^+$) (Figure 1a). Ultrafast transient absorption (TA) spectroscopy was acquired to accurately identify the distribution of different-n phases in Q-2D perovskites films with different cations substituting (**Figure 3**a–c; Figure S6, Supporting Information). Analogous to PEA-film, there are four distinct photobleaching (PB) peaks at 435, 462, 483, and 500 nm, belonging to $n = 2$, 3, 4, and $n \geq 5$ phase, respectively, shown in the TA spectra of DPPA/PEA and DPEA/PEA-perovskites at different timescales (Figure 3a,b). However, compared with PEA-film, the signals of low-n (especially $n = 2$) phases are obviously weak-

ened, meaning suppressed phase segregation.[38] Furthermore, it is noteworthy that only one dominant PB peak >500 nm, assigned to the high-n ($n \geq 5$) phase, is observed in the TA spectra of TPMA/PEA-film. To vividly display the phase distribution, we plot the contribution of different-n phases according to the integral intensity of PB peaks in the corresponding TA spectra in the insets of Figure 3a–c. The low-n ($n = 2$, 3, 4) phases are significantly reduced in the DPPA/PEA and DPEA/PEA films and finally disappear in the TPMA/PEA film.

Monitoring the evolution of phase distribution in situ further confirms the conception that the assembly of spacer cations at the nucleation stage is decisive to the n-phase distribution and the "co-assembly" of spacer cations is disturbed more severely when incorporating bulkier cations (Figure 3d–i). Consistent with the results in Figure 2, the absorption intensity of low-n phases remains approximately constant throughout the fabrication

ADVANCED
SCIENCE NEWS

www.advancedsciencenews.com
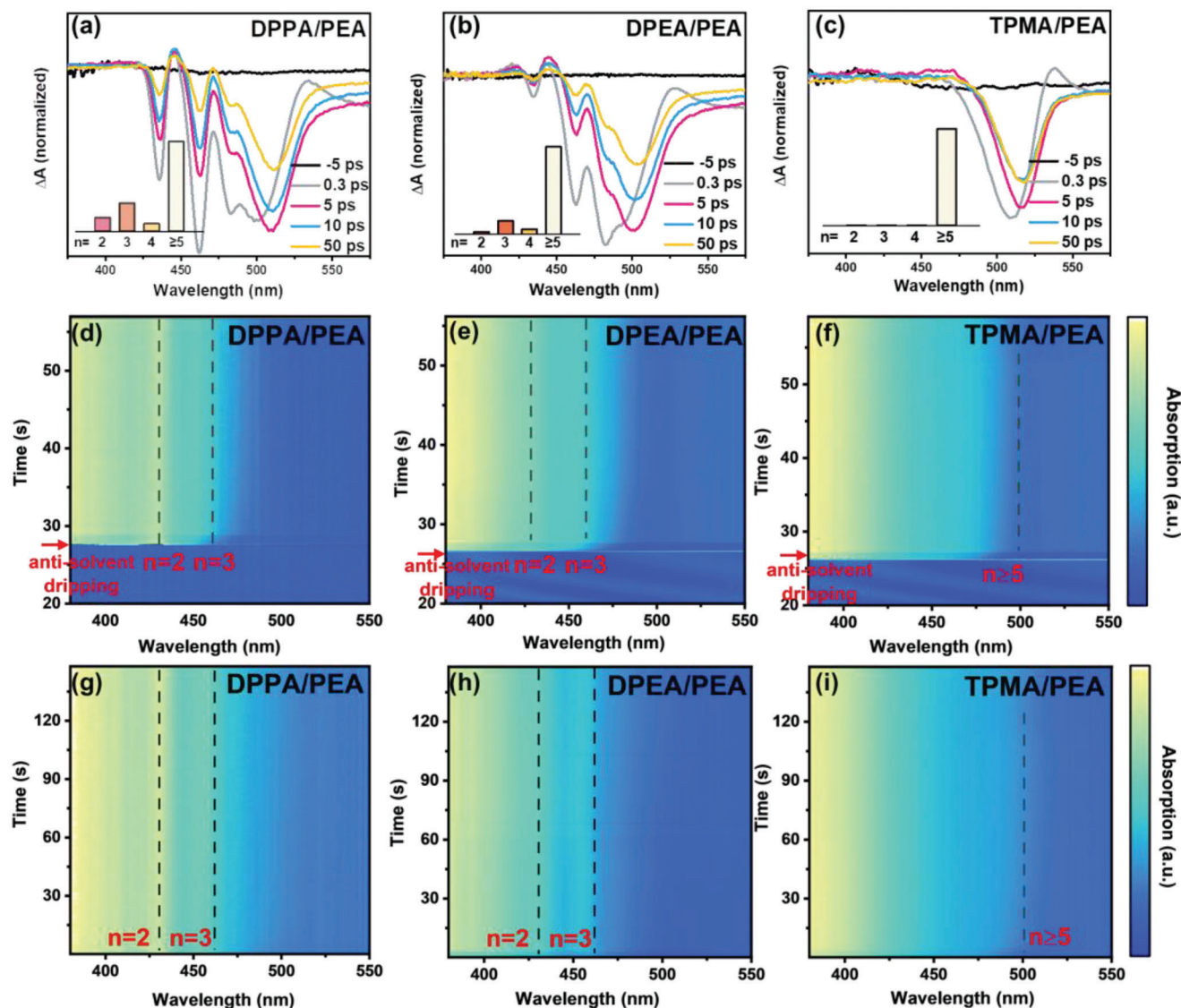
ADVANCED
MATERIALS

www.advmat.de

Figure 3. a–c) Transient absorption spectra of Q-2D perovskites with different spacer cations substitution. The inset in (a–c) represents the relative contributions of different n phases in each film according to the integral intensity of GSB in the corresponding TA spectra. d–i) In situ absorbance measurement of Q-2D perovskites with different spacer cations substitution during spin coating (d–f) and annealing (g–i) process.

process, indicating the phase distribution is determined at the moment when the anti-solvent drop. Besides, **Figure 4**a,b are plots of absorption intensity of $n = 2$ phase versus time during spin coating (Figure 4a) and annealing (Figure 4b) process. The corresponding in situ absorbance measurements and absorption over time with IBA$^+$ and tBA$^+$ substitution are shown in Figures S7–S10 (Supporting Information). Except for the unchanged absorption intensity over time, it is also observed that the content (absorption intensity) of $n = 2$ phase is in the order of IBA$^+$ > IPA$^+$ > tBA$^+$ and DPPA$^+$ > DPEA$^+$ > TPMA$^+$, among which TPMA/PEA-sample possess the fewest, indicative of the close correlation with the molecular configuration.

Based on the above discussion, we describe the mechanism of regulating phase distribution in the schematic diagram in Figure 4c, the bulkier the co-cations, the weaker the stacking of PEA$^+$, contributing to quantum wells with higher-n phase

and homogeneous phase distribution. The crystallization of perovskite crystals involves the diffusion and arrangement of perovskite components in precursor,[31,32] which together account for the assembling behaviors. However, in one-step methods, the majority of DMSO is extracted swiftly by anti-solvent CB, where supersaturation of solute is reached so fast that the perovskite components subsequently assemble into domains with different quantum well widths. As a result, the arrangement of the perovskite component, rather than the diffusion, dominates the nucleation state such that PEA$^+$ assemble as a spacer layer preferentially due to strong π–π stacking, resulting in quantum wells with low-n phases and severe phase segregation. However, mixing cations with different assembling abilities pose a steric hindrance for spacer cations aggregation, leaving the formation of fewer low-n phases in the nucleation stage.[28] Furthermore, incorporating cations with even bulkier tails like TPMA$^+$ will

**ADVANCED
SCIENCE NEWS**

www.advancedsciencenews.com
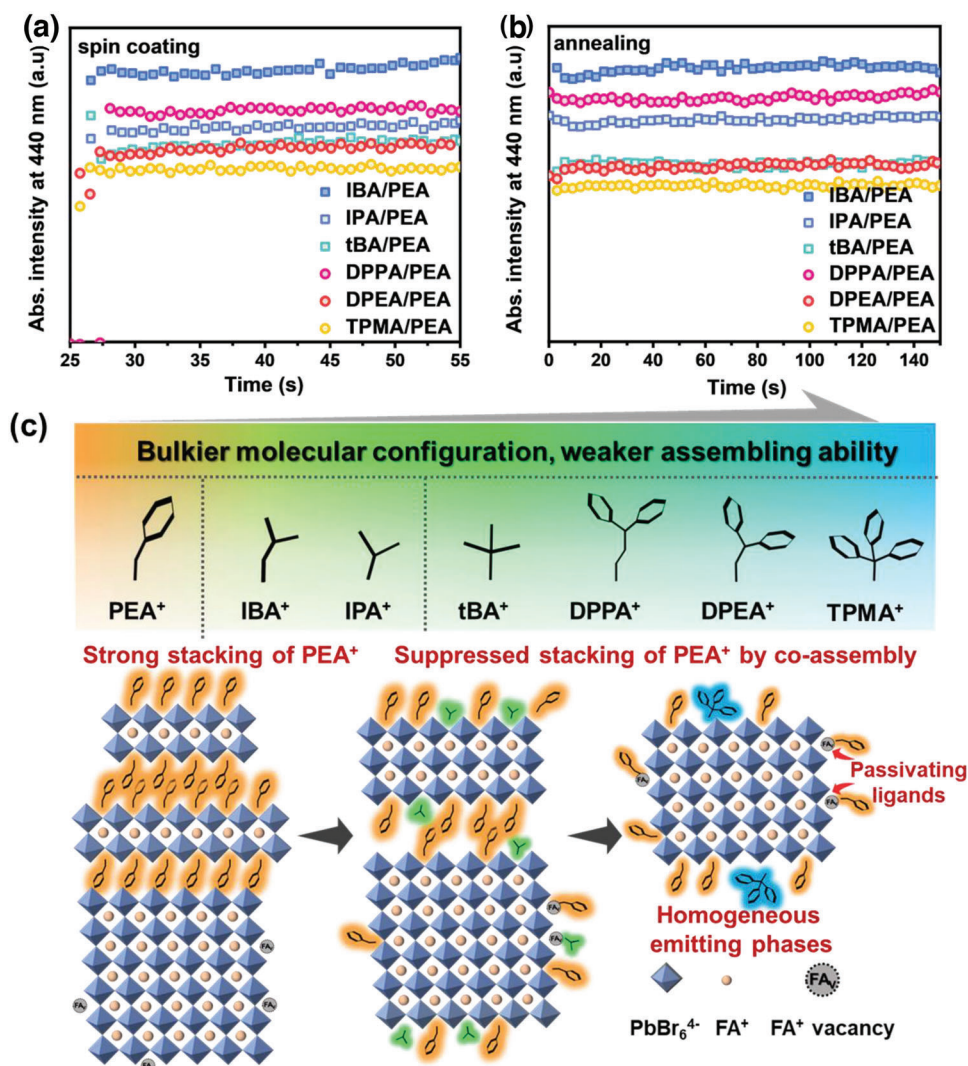
**ADVANCED
MATERIALS**

www.advmat.de

Figure 4. a,b) Evolution of absorption at 440 nm over time in Q-2D perovskites with different spacer cations substitution during spin coating (a) and annealing (b) process. c) Schematic diagram of the impacts of spacer cations with different sizes and configurations on the crystallization kinetics of Q-2D perovskites.

eliminate the formation of low-n phases, realizing a homogeneous phase distribution and passivation of cation ligands simultaneously. Therefore, we conclude that it is the arrangement, rather than diffusion, of spacer cations that influence the assembling behaviors at the nucleation stage, which determine the resultant phase distribution.

2.4. Performance of the Corresponding Q-2D Perovskite LEDs

The substitution of TPMA$^+$ realizes a homogeneous n-phase distribution, which will potentially reduce the energy loss during energy transfer. Thus, we assess the luminescent properties of Q-2D perovskite films through a series of characterization (**Figure 5**a–c). PL spectra (Figure 5a) only exhibit a dominant emission peak at 530 nm, where a significant augment in PL intensity exists in the TPMA/PEA sample, indicating promoted radiative recombination. In addition, normalized PL spectra in

logarithmic coordinates shown as dashed lines (Figure 5a) exhibit distinct differences, where peaks at 440 and 470 nm ($n = 2$ and 3 phases, respectively), originally existing in PEA- sample, disappear in the TPMA/PEA sample. Meanwhile, XRD patterns (Figure S11, Supporting Information) also show that the diffraction signal of the low-n ($n = 2$) phase almost disappears, indicating the absence of low-n phases. Figure 5b shows the time-resolved photoluminescence (TRPL) results. The fitted average PL lifetime increased from 43.3 ns (PEA) to 115.7 ns (TPMA/PEA), indicating suppressed defects and favored radiative recombination, which agrees with the space charge-limited current (SCLC) measurements in Figure S12 (Supporting Information). Accordingly, the PLQY of Q-2D perovskite films (Figure 5c) increase significantly from 65.4% (PEA) to 81.2% (TPMA/PEA). We compare the confinement effect of PEA$^+$ and TPMA$^+$ on perovskite growth based on $<n> = 3$ composition with single spacer cation (Figure S13a,b, Supporting Information, detailed compositions are listed in inset.). As shown in

**ADVANCED
SCIENCE NEWS**
www.advancedsciencenews.com
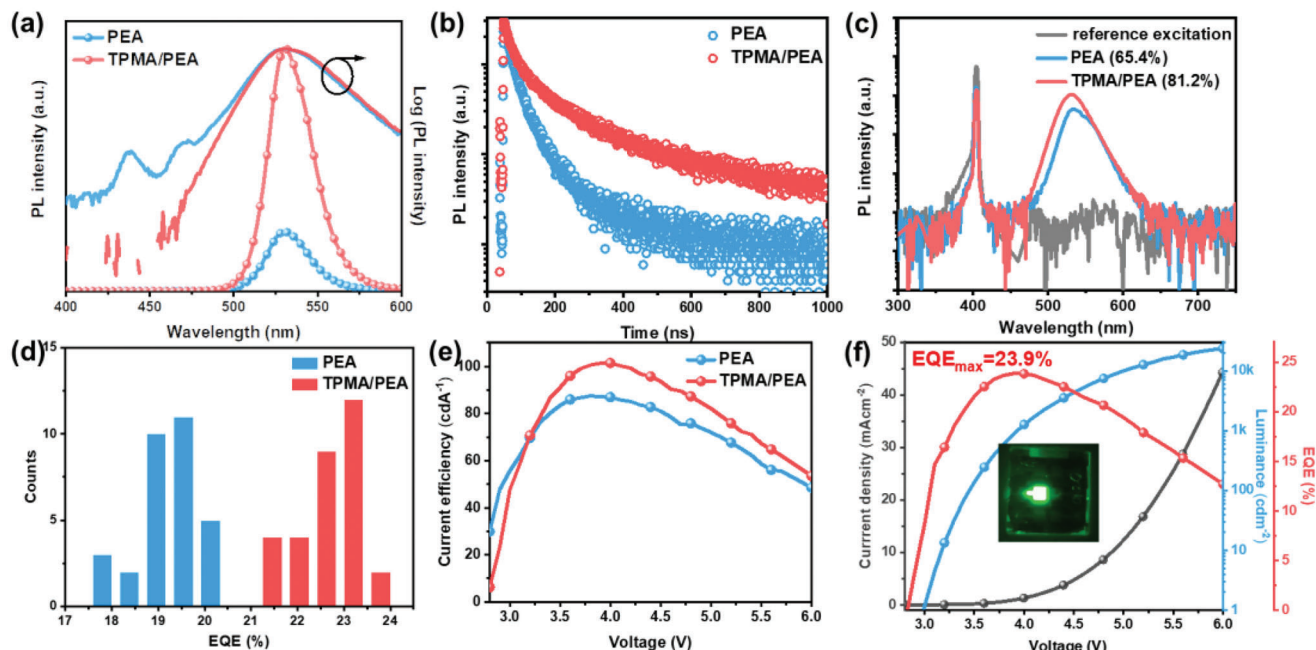
**ADVANCED
MATERIALS**
www.advmat.de

Figure 5. a) PL spectra, b) time-resolved photoluminescence (TRPL), and c) photoluminescence quantum yield (PLQY) of Q-2D perovskites films without and with TPMA$^+$ substitution. d) Histogram of maximum EQE measured from 31 devices without and with TPMA$^+$ substitution. e) Current efficiency–voltage (CE–V) curves of the Q-2D perovskite LED devices without and with TPMA$^+$ substitution. f) J–V–L–EQE curves of the champion device with TPMA$^+$ substitution.

Figure S13a (Supporting Information), the absorption edge of the TPMA film obviously red-shift compared with the PEA film. Meanwhile, the PL spectra (Figure S13b, Supporting Information) of FAPbBr$_3$, PEA- and TPMA-film exhibit PL peak at 540, 530, and 537 nm, respectively, which means a stronger confinement effect of PEA$^+$ than TPMA$^+$. The confinement effect is closely related to the binding affinity between spacer cations and lead halogen frameworks, where higher binding affinity leads to stronger confinement.[37] Therefore, we propose that TPMA$^+$ exhibit a lower tendency to bind with lead halogen frameworks and it is the slender cation PEA$^+$ that binds the perovskite surface firmly. In the film employing a co-assembly strategy (TPMA/PEA-film), the emitting phase is more effectively passivated by PEA$^+$, which otherwise assembles into a spacer layer of low-n phases. Scanning electron microscopy (SEM) was applied to investigate the morphology of Q-2D perovskite films. As shown in Figure S14 (Supporting Information), both films possess full coverage with corrugated structures, which is consistent with previous documents, indicating great potential for light-emitting diodes (LEDs) applications.[31]

Therefore, we fabricated Q-2D perovskite LEDs based on the device structure of ITO/ modified PEDOT: PSS/Q-2D perovskites/TPBi/ LiF/Al. The hole transport layer is modified by mixing diluted PEDOT: PSS with poly (sodium 4-styrenesulfonate) aqueous solution (Experimental Section).[17] Figure S15 (Supporting Information) plots the electroluminescence spectra of the TPMA/PEA device, which exhibits emission at 530 nm and no shift under higher voltages. Figure 5e are the plots of current efficiency (CE) versus voltage for PEA and TPMA/PEA-LED devices. The highest CE increase was from 87.5 cd A^{-1} (PEA) to 101.5 cd A^{-1} (TPMA/PEA). The correspond-

ing champion EQE of TPMA/PEA-device reached 23.9%, which is among the highest efficiency of green Q-2D perovskite LEDs. Figure 5f shows the J–V–L–EQE curves of the champion device. The turn-on voltage is below 3.0 V and the highest luminance reaches 23 657 cd m^{-2}. Figure 5d is the histogram of maximum EQE measured from 31 PEA and TPMA/PEA devices. The highest EQE increases from 20.3% (PEA) to 23.9% (TPMA/PEA) and the average EQE is 19.24% (PEA) and 22.6% (TPMA/PEA), respectively, exhibiting good reproducibility of our devices. The EL performance of the devices based on pure TPMA, DPPA/PEA, and DPEA/PEA films are also given in Figure S16 (Supporting Information). In addition, we also assess the operational stability of our LED devices with an initial luminance (L$_0$) of ≈100 cd m^{-2} (initial EQE of 18% and 22% for PEA and TPMA/PEA, respectively). As shown in Figure S17a (Supporting Information), the T$_{50}$ (time required for the EL intensity and EQE to reach 50% of its initial value) increases from ≈30 min (PEA) to 70 min (TPMA/PEA), which we ascribe to passivated defects in TPMA/PEA-films. Further discussion regarding the reliable behavior of the devices when subjected to multiple IV sweeps is included in Figure S17b–h (Supporting Information). The instability of perovskite photoelectric device is mainly due to the migration of ions under electric fields, which is related to the ionic crystal properties of perovskites. The migration of ions is easier to happen in Q-2D perovskites obtained from the one-step method because the emitting phase ($n\rightarrow\infty$) is in situ formed nanocrystal embedded within organic ligands, lacking close alignment between the isolated crystals,[21,41,42] which makes it fragile under electric field. The capped cation ligands cannot fundamentally restrict the severe migration of anions (Br$^-$) under an electric field. Moreover, the limited thickness (<100 nm) of Q-2D perovskite

**ADVANCED
SCIENCE NEWS**

www.advancedsciencenews.com

**ADVANCED
MATERIALS**

www.advmat.de

film increases the pressure of the electric field under the same voltage. Therefore, the lifetime of Q-2D perovskite LEDs is still limited compared with 3D perovskite LEDs.[7,37] Strategies like interface engineering, core-shell structure, device structure engineering and so on are needed to overcome the instability of perovskite LED in the future.

3. Conclusion

We have revealed the formation kinetics of width distribution of quantum well in Q-2D perovskites via in situ absorbance spectroscopy, where phase distribution is primarily governed by the arrangement, rather than diffusion, of spacer cations at the nucleation stage, which associate with the assembling ability of spacer cations. Moreover, the assembling ability associated with a molecular configuration that cations with bulkier and more branching alkyl terminals render weaker assembly and pose a steric hindrance for cations aggregation. Therefore, we realize homogeneous phase distribution in the PEA$^+$-based Q-2D perovskites ($<n>$ = 3) via a "co-assembly" strategy by incorporating branching TPMA$^+$, to suppress cations aggregation in low-n phases and afford adequate cations as passivating ligands for emitting phases. Correspondingly, the PLQY of the perovskite films significantly increase from 65.4% (pristine) to 81.2% and the EQE of the LED device reach 23.9%, which is among the highest performance of green Q-2D perovskite LEDs. This work shed light on the formation process of multiphase in Q-2D perovskites and emphasizes the designing principle of spacer cations to regulate phase distribution, providing further guidance on the modulation of Q-2D perovskites.

4. Experimental Section

Materials: Lead bromide (PbBr$_2$), potassium bromide (KBr), poly (sodium 4-styrenesulfonate) (PSS-Na, average $M_w \approx 70\ 000$), dimethyl sulfoxide (DMSO), and chlorobenzene (CB) were purchased from Sigma Aldrich. 2,2′,2″-(1,3,5-Benzinetriyl)-*tris*(1-phenyl-1-H-benzimidazole) (TPBi), formamidinium bromide (FABr), methylammonium chlorine (MACl) and phenethylamine bromide (PEABr) were purchased from Xi'an Polymer Light Technology Corp. Lithium fluoride (LiF, 99.99%) was purchased from Alfa Aesar. Bromine salts of different amines used were synthesized by the reaction between amines and hydrobromic (HBr) reported elsewhere.

Device Fabrication: The ITO substrates were sequentially cleaned by sonication in deionized water, acetone, and isopropyl alcohol. Diluted PEDOT: PSS (PEDOT: PSS: H$_2$O v:v = 1:1) and PSS-Na aqueous solution (15 mg mL^{-1}) were mixed and stirred overnight. The optimized volume ratio between diluted PEDOT: PSS and PSS-Na aqueous solution was 1:0.6 and 1:0.8 for PEA- and TPMA/PEA-device, respectively. The modified PEDOT: PSS aqueous solution was spin-coated onto the ITO substrates at 4000 rpm for 35 s and annealed at 150 °C for 20 min in ambient air. The perovskite precursor solutions were prepared by dissolving PbBr$_2$ (146.8 mg), FABr (33.3 mg), PEABr (53.9 mg), MACl (2.7 mg), and KBr (16 mg) in 1 mL DMSO under continuous stirring for 2 h at 70 °C. The precursor solutions with other ammoniums were prepared by substituting different molar ratios (0, 0.3, 0.7) of PEA$^+$ with other ammonium bromides. All precursor solutions were filtered through 0.22 μm filter before use. Then the perovskite films were prepared in a N$_2$ glovebox. The perovskite precursor solution was spin-coated onto the substrates via a two-step spin coating process at 1000 and 3000 rpm for 10 and 60 s, respectively. After spin coating for 30 s during the second step, 400 μL of chlorobenzene (CB)

was poured onto the perovskite films. Then the perovskite films were annealed at 90 °C for 60 min. For passivation, 1.8 mg mL^{-1} TOPO in CB was spin-coated on the perovskite films at 7000 rpm for 1 min. Finally, the TPBi (40 nm), LiF (1 nm), and Al electrode (100 nm) were deposited sequentially through a thermal evaporator. The device area was 0.045 cm^2 defined by the overlapping area of ITO and Al electrode.

Characterization: In situ, UV–vis absorption spectra were recorded on a commercialized dynamic spectrometer system (Du-100, Puguangweishi Co. Ltd) in a nitrogen-filled glovebox. A simplified setup of the test system was described below (Figure S18, Supporting Information). First, one blank substrate was used to get the baseline. As for in situ measurement during spin-coating (Figure S18a, Supporting Information), one optical fiber linking to the detector was set through the hole in the chuck of the spin-coater. The probe beam from the Xenon lamp passed through the substrate and the hole in the chuck sequentially got to the detector and analyzed the evolution of the light intensity of the selected wavelength. The perovskite precursor was dropped onto the substrate and anti-solvent was poured onto the center of the substrate diagonally. On the other hand, a custom-built hot plate, with a tiny hole for light passing, connecting to a heater and temperature sensor was used to conduct the in situ measurement during annealing (Figure S18b, Supporting Information). Likewise, the probe beam passed through the perovskite film, substrate, and the hole in the plate sequentially, got to the detector and analyzed the evolution of the light intensity of selected wavelength. Photoluminescence (PL) was measured by FLS980 (Edinburgh Instruments Ltd) with an excitation at 340 nm. The UV–vis absorption spectra of the samples was obtained by a UV–vis diffuse reflectance spectrophotometer (UV–vis DRS, Japan Hitachi UH4150). Transient absorption spectroscopy was conducted by using a commercial TA spectrometer (Helios, Ultrafast Systems). The output of an optical parametric amplifier (Opera Solo, Coherent) coupled with an 800 nm, 1 kHz amplified Ti: sapphire laser system (Astrella, Coherent) was used as the pump beam (100 fs). The pump wavelength was 360 nm. The probe beam was a white light continuum beam spanning from 360 to 700 nm, which was created by focusing 0.1% of the 800 nm fundamental output onto a sapphire crystal. All the samples were encapsulated with quartz flakes during these optical measurements. The methods to calculate the relative contributions of different phases were applied according to previous reports.[26,38] The relative presence of each phase was quantified by the amplitude of the transient absorption signal at t = 0.3 ps, during which the energy transfer had not happened and the intensity of PB peaks represented the populations of corresponding phases. The PLQYs of the perovskite films were recorded by a commercialized PLQY measurement system from Enlitech with excitation from a 405 nm LED. The XRD patterns were collected by using a PANalytical X'Pert Pro X-ray powder diffractometer with Cu Kα radiation (λ = 1.54050 Å). The morphology was measured by a SEM (S4800). The GIWAXS data were obtained at beamline BL14B1 of the Shanghai Synchrotron Radiation Facility using X-ray with a wavelength of 0.6887 Å. The J–V–L curve, EQE and operational stability measurement of the perovskite LEDs and the PLQY measurement was conducted using a commercialized system (LQE-100-EL, Enlitech) equipped with an integrated sphere and a photomultiplier tube (PMT), in which the PMT was used to measure the low luminance up to 10^{-4} cd m^{-2}, ensuring accurate measurement of luminance. All the device characterization tests of perovskite LEDs were recorded at room temperature in the N2-filled glovebox for the unencapsulated devices.

DFT Calculations: To obtain the interaction and binding features between organic molecules and lead–bromine sheet. The geometric structures of individual molecules were optimized, the lead–bromine sheet, and the combinations of them, respectively, by using DFT as implemented in the Vienna ab initio simulation package.[43] The Perdew–Burke–Ernzerhof (PBE) functional within the generalized gradient approximation[44] was used to treat the exchange-correlation between electrons, and the projector augmented wave pseudopotential[45] was used to desribe the interaction between ionic cores and valence electrons. The (001) surface of the substrate was used for the intercalation of the organic molecules. A supercell of 2 × 2 × 1 unit cells of the substrate was used to avoid the influence of the periodic boundary condition. Monkhorst-Pack k-meshes[46] with a grid density of 2π × 0.05 Å^{-1} were used to sample the first Brillouin zone.

For geometry optimization, the cutoff energy for the plane-wave basis set was set to 500 eV, and the convergence thresholds for the total energy and force were set as 10^{-5} eV and 0.05 eV Å^{-1}, respectively. The DFT-D2 correction[47] was applied to deal with the long-range van der Waals interactions. The adsorption energies (E_{ads}) of organic molecules on the substrate were calculated by using the following equation:

$$E_{ads} = E(\text{mol} + \text{sub}) - n \times E(\text{mol}) - E(\text{sub}) \tag{1}$$

where $E(\text{mol})$, $E(\text{sub})$, and $E(\text{mol} + \text{sub})$ are the energies of the organic molecule, the lead–bromine sheet, and the combinations of them, n is the number of molecules adsorbed on the substrates per cell.

Supporting Information

Supporting Information is available from the Wiley Online Library or from the author.

Conflict of Interest

The authors declare no conflict of interest.

Data Availability Statement

Research data are not shared.

Keywords

[1] H. Cho, S.-H. Jeong, M.-H. Park, Y.-H. Kim, C. Wolf, C.-L. Lee, J. H. Heo, A. Sadhanala, N. Myoung, S. Yoo, *Science* **2015**, *350*, 1222.

[2] Z. K. Tan, R. S. Moghaddam, M. L. Lai, P. Docampo, R. Higler, F. Deschler, M. Price, A. Sadhanala, L. M. Pazos, D. Credgington, F. Hanusch, T. Bein, H. J. Snaith, R. H. Friend, *Nat. Nanotechnol.* **2014**, *9*, 687.

[3] Y. Cao, N. Wang, H. Tian, J. Guo, Y. Wei, H. Chen, Y. Miao, W. Zou, K. Pan, Y. He, H. Cao, Y. Ke, M. Xu, Y. Wang, M. Yang, K. Du, Z. Fu, D. Kong, D. Dai, Y. Jin, G. Li, H. Li, Q. Peng, J. Wang, W. Huang, *Nature* **2018**, *562*, 249.

[4] K. Lin, J. Xing, L. N. Quan, F. De Arquer, X. Gong, J. Lu, L. Xie, W. Zhao, D. Zhang, C. Yan, *Nature* **2018**, *562*, 245.

[5] D. Ma, K. Lin, Y. Dong, H. Choubisa, A. H. Proppe, D. Wu, Y.-K. Wang, B. Chen, P. Li, J. Z. Fan, F. Yuan, A. Johnston, Y. Liu, Y. Kang, Z.-H. Lu, Z. Wei, E. H. Sargent, *Nature* **2021**, *599*, 594.

[6] S.-J. Woo, J. S. Kim, T.-W. Lee, *Nat. Photonics* **2021**, *15*, 630.

[7] J. S. Kim, J. M. Heo, G. S. Park, S. J. Woo, C. Cho, H. J. Yun, D. H. Kim, J. Park, S. C. Lee, S. H. Park, E. Yoon, N. C. Greenham, T. W. Lee, *Nature* **2022**, *611*, 688.

[8] X. K. Liu, W. Xu, S. Bai, Y. Jin, J. Wang, R. H. Friend, F. Gao, *Nat. Mater.* **2021**, *20*, 10.

[9] M. Vasilopoulou, A. Fakharuddin, F. P. García de Arquer, D. G. Georgiadou, H. Kim, A. R. b. m. Yusoff, F. Gao, M. K. Nazeeruddin, H. J. Bolink, E. H. Sargent, *Nat. Photonics* **2021**, *15*, 656.

[10] C. Qin, A. S. D. Sandanayaka, C. Zhao, T. Matsushima, D. Zhang, T. Fujihara, C. Adachi, *Nature* **2020**, *585*, 53.

[11] C. Qin, T. Matsushima, W. J. Potscavage, A. S. D. Sandanayaka, M. R. Leyden, F. Bencheikh, K. Goushi, F. Mathevet, B. Heinrich, G. Yumoto, Y. Kanemitsu, C. Adachi, *Nat. Photonics* **2019**, *14*, 70.

[12] M. Yuan, L. N. Quan, R. Comin, G. Walters, R. Sabatini, O. Voznyy, S. Hoogland, Y. Zhao, E. M. Beauregard, P. Kanjanaboos, *Nat. Nanotechnol.* **2016**, *11*, 872.

[13] Y. Jiang, M. Cui, S. Li, C. Sun, Y. Huang, J. Wei, L. Zhang, M. Lv, C. Qin, Y. Liu, M. Yuan, *Nat. Commun.* **2021**, *12*, 336.

[14] X. Yang, X. Zhang, J. Deng, Z. Chu, Q. Jiang, J. Meng, P. Wang, L. Zhang, Z. Yin, J. You, *Nat. Commun.* **2018**, *9*, 570.

[15] C. Sun, Y. Jiang, M. Cui, L. Qiao, J. Wei, Y. Huang, L. Zhang, T. He, S. Li, H. Y. Hsu, C. Qin, R. Long, M. Yuan, *Nat. Commun.* **2021**, *12*, 2207.

[16] W. Dong, X. Zhang, F. Yang, Q. Zeng, W. Yin, W. Zhang, H. Wang, X. Yang, S. V. Kershaw, B. Yang, A. L. Rogach, W. Zheng, *ACS Nano* **2022**, *16*, 9679.

[17] X. Peng, X. Yang, D. Liu, T. Zhang, Y. Yang, C. Qin, F. Wang, L. Chen, S. Li, *ACS Energy Lett.* **2021**, *6*, 4187.

[18] J. Cui, Y. Liu, Y. Deng, C. Lin, Z. Fang, C. Xiang, P. Bai, K. Du, X. Zuo, K. Wen, *Sci. Adv.* **2021**, *7*, eabg8458.

[19] S. C. Liu, Z. Y. Guo, X. X. Wu, X. F. Liu, Z. J. Huang, L. Li, J. W. Zhang, H. P. Zhou, L. D. Sun, C. H. Yan, *Adv. Mater.* **2022**, *35*, 2208078.

[20] J. Qing, S. Ramesh, Q. Xu, X. K. Liu, H. Wang, Z. Yuan, Z. Chen, L. Hou, T. C. Sum, F. Gao, *Adv. Mater.* **2021**, *33*, 2104381.

[21] Z. Liu, W. Qiu, X. Peng, G. Sun, X. Liu, D. Liu, Z. Li, F. He, C. Shen, Q. Gu, F. Ma, H. L. Yip, L. Hou, Z. Qi, S. J. Su, *Adv. Mater.* **2021**, *33*, 2103268.

[22] C. Zhao, W. Wu, H. Zhan, W. Yuan, H. Li, D. Zhang, D. Wang, Y. Cheng, S. Shao, C. Qin, L. Wang, *Angew. Chem., Int. Ed.* **2022**, *61*, e202117374.

[23] J. Jiang, Z. Chu, Z. Yin, J. Li, Y. Yang, J. Chen, J. Wu, J. You, X. Zhang, *Adv. Mater.* **2022**, *34*, 2204460.

[24] Z. Guo, Y. Zhang, B. Wang, L. Wang, N. Zhou, Z. Qiu, N. Li, Y. Chen, C. Zhu, H. Xie, T. Song, L. Song, H. Xue, S. Tao, Q. Chen, G. Xing, L. Xiao, Z. Liu, H. Zhou, *Adv. Mater.* **2021**, *33*, 2102246.

[25] Y. K. Wang, D. Ma, F. Yuan, K. Singh, J. M. Pina, A. Johnston, Y. Dong, C. Zhou, B. Chen, B. Sun, H. Ebe, J. Fan, M. J. Sun, Y. Gao, Z. H. Lu, O. Voznyy, L. S. Liao, E. H. Sargent, *Nat. Commun.* **2020**, *11*, 3674.

[26] L. N. Quan, Y. Zhao, F. P. Garcia de Arquer, R. Sabatini, G. Walters, O. Voznyy, R. Comin, Y. Li, J. Z. Fan, H. Tan, J. Pan, M. Yuan, O. M. Bakr, Z. Lu, D. H. Kim, E. H. Sargent, *Nano Lett.* **2017**, *17*, 3701.

[27] D. Z. Zhang, Y. X. Fu, C. Y. Liu, C. Y. Zhao, X. Gao, J. D. Zhang, W. B. Guo, J. Liu, C. J. Qin, L. X. Wang, *Adv. Funct. Mater.* **2021**, *31*, 2103890.

[28] J. Xing, Y. Zhao, M. Askerka, L. N. Quan, X. Gong, W. Zhao, J. Zhao, H. Tan, G. Long, L. Gao, Z. Yang, O. Voznyy, J. Tang, Z. H. Lu, Q. Xiong, E. H. Sargent, *Nat. Commun.* **2018**, *9*, 3541.

[29] C. Liang, H. Gu, Y. Xia, Z. Wang, X. Liu, J. Xia, S. Zuo, Y. Hu, X. Gao, W. Hui, L. Chao, T. Niu, M. Fang, H. Lu, H. Dong, H. Yu, S. Chen, X. Ran, L. Song, B. Li, J. Zhang, Y. Peng, G. Shao, J. Wang, Y. Chen, G. Xing, W. Huang, *Nat. Energy* **2020**, *6*, 38.

[30] T. Cheng, C. J. Qin, S. Watanabe, T. Matsushima, C. Adachi, *Adv. Funct. Mater.* **2020**, *30*, 2001816.

[31] R. Quintero-Bermudez, A. Gold-Parker, A. H. Proppe, R. Munir, Z. Yang, S. O. Kelley, A. Amassian, M. F. Toney, E. H. Sargent, *Nat. Mater.* **2018**, *17*, 900.

[32] L. Liu, Y. Bai, X. Zhang, Y. Shang, C. Wang, H. Wang, C. Zhu, C. Hu, J. Wu, H. Zhou, Y. Li, S. Yang, Z. Ning, Q. Chen, *Angew. Chem., Int. Ed.* **2020**, *59*, 5979.

[33] M. Ban, Y. Zou, J. P. Rivett, Y. Yang, T. H. Thomas, Y. Tan, T. Song, X. Gao, D. Credgington, F. Deschler, *Nat. Commun.* **2018**, *9*, 3892.

[34] L. Kong, X. Zhang, Y. Li, H. Wang, Y. Jiang, S. Wang, M. You, C. Zhang, T. Zhang, S. V. Kershaw, *Nat. Commun.* **2021**, *12*, 1246.

[35] H. Chen, S. Teale, B. Chen, Y. Hou, L. Grater, T. Zhu, K. Bertens, S. M. Park, H. R. Atapattu, Y. J. Gao, M. Y. Wei, A. K. Johnston, Q. L. Zhou, K. M. Xu, D. N. Yu, C. C. Han, T. Cui, E. H. Jung, C. Zhou, W. J. Zhou, A. H. Proppe, S. Hoogland, F. Laquai, T. Filleter, K. R. Graham, Z. J. Ning, E. H. Sargent, *Nat. Photonics* **2022**, *16*, 352.

[36] J. Ovčar, T. L. Leung, L. Grisanti, Ž. Skoko, M. Vrankić, K.-H. Low, S. Wang, P.-Y. You, H. Ahn, I. Lončarić, A. B. Djurišić, J. Popović, *Chem. Mater.* **2022**, *34*, 4286.

[37] Y. Jiang, C. Sun, J. Xu, S. Li, M. Cui, X. Fu, Y. Liu, Y. Liu, H. Wan, K. Wei, T. Zhou, W. Zhang, Y. Yang, J. Yang, C. Qin, S. Gao, J. Pan, Y. Liu, S. Hoogland, E. H. Sargent, J. Chen, M. Yuan, *Nature* **2022**, *612*, 679.

[38] C. Wang, D. Han, J. Wang, Y. Yang, X. Liu, S. Huang, X. Zhang, S. Chang, K. Wu, H. Zhong, *Nat. Commun.* **2020**, *11*, 6428.

[39] C. Wang, G. Dai, J. Wang, M. Cui, Y. Yang, S. Yang, C. Qin, S. Chang, K. Wu, Y. Liu, H. Zhong, *Nano Lett.* **2022**, *22*, 1338.

[40] Y. Zhang, M. Sun, N. Zhou, B. Huang, H. Zhou, *J. Phys. Chem. Lett.* **2020**, *11*, 7610.

[41] Y. Liu, J. Cui, K. Du, H. Tian, Z. He, Q. Zhou, Z. Yang, Y. Deng, D. Chen, X. Zuo, Y. Ren, L. Wang, H. Zhu, B. Zhao, D. Di, J. Wang, R. H. Friend, Y. Jin, *Nat. Photonics* **2019**, *13*, 760.

[42] L. Zhao, Y. W. Yeh, N. L. Tran, F. Wu, Z. Xiao, R. A. Kerner, Y. L. Lin, G. D. Scholes, N. Yao, B. P. Rand, *ACS Nano* **2017**, *11*, 3957.

[43] G. Kresse, J. Furthmüller, *Phys. Rev. B* **1996**, *54*, 11169.

[44] J. P. Perdew, K. Burke, M. Ernzerhof, *Phys. Rev. Lett.* **1996**, *77*, 3865.

[45] P. E. Blöchl, *Phys. Rev. B* **1994**, *50*, 17953.

[46] H. J. Monkhorst, J. D. Pack, *Phys. Rev. B* **1976**, *13*, 5188.

[47] S. Grimme, *J. Comput. Chem.* **2006**, *27*, 1787.